

# Digital Light Processing of 2D Lattice Composites for Tunable Self-Sensing and Mechanical Performance

Omar Waqas Saadi, Mohammed Ayaz Uddin, Andreas Schiffer,\*  
and Shanmugam Kumar\*

This study investigates the mechanical and piezoresistive self-sensing performance of additive manufacturing-enabled 2D nanocomposite lattices under monotonic and cyclic tensile loading. Lattice structures comprising hexagonal, chiral, triangular, and reentrant unit cell topologies are realized via digital light processing using an acrylic photocurable resin filled with carbon nanotubes (CNTs). The results reveal that the piezoresistive sensitivity of reentrant and triangular lattices is nearly insensitive to changes in relative density. In contrast, the gauge factors of the hexagonal and chiral lattices rise by 300% and 500%, respectively, with an increase in relative density from 20 to 40%, which can be ascribed to their bend-dominated behavior, causing an increase in surface strains in the lattice struts with increasing relative density for an imposed macroscopic strain. The measured stress versus strain responses compare well with nonlinear finite element results. Under strain-controlled cyclic loading, the electrical resistance of the 2D lattices is found to decline over time due to reorientation of the CNTs in the surrounding viscoelastic polymer matrix. The findings provide valuable insights into the interrelations between sensing performance, cell architecture, and relative density of the lattices, and offer guidelines for the design of architected strain sensors and self-sensing lightweight structures.

and engineering due to their necessity for many practical applications. For many years, advances in materials science relied on modifying composition (alloying or compositing) and/or microstructure through processing to improve the mechanical and/or functional properties of materials. Although effective, it typically takes years for a newly developed material to reach the market. A large window of materials allows us to select appropriate material(s) according to application requirements.<sup>[1]</sup> Many materials found in nature depict a remarkable combination of different properties that are not often mutually inclusive in practice. Over millions of years of evolution, natural materials—and cellular materials in particular—have perfected an optimal architecture that spans several hierarchies and length scales.<sup>[2]</sup> Natural cellular materials possess periodic or stochastic formations of open or closed cells and two-dimensional cell topologies or three-dimensional polyhedral structures, depending on the type/family

of material.<sup>[3,4]</sup> Honeycombs, sponges, wood, and cork are all examples of cellular solids that can be found in nature.<sup>[4]</sup> The idea of merging cellular architecture with materials is not new, but it is gaining traction as alloying and compositing pose fundamental limitations to widening property space.

Lattice materials are created by periodically patterning their distinctive unit cell in space and are consisting of a large number of well-defined, architecturally designed structural members like beams, rods, plates, or shells. Lattices can be classified as open or closed cell structures that may exhibit stretch-dominance or bend-dominance in their deformation.<sup>[4]</sup> From a materials engineering perspective, the mechanical properties of lattice structures have been extensively studied in relation to their topology and relative density.<sup>[4,5]</sup> However, it is less known how their functional properties (e.g., electrical, thermal, and magnetic properties) relate to the lattice topology and relative density. This is partly due to the complexity of the underlying mechanisms that control functional properties, as well as the difficulty in controlling and characterizing these properties in lattice structures.


In recent years, advances in fabrication techniques and characterization methods have allowed for more detailed studies of functional properties in lattice structures. Researchers are now

## 1. Introduction

The properties of materials have long been one of the most foundational and are intensively being explored in materials science

O. W. Saadi, M. A. Uddin, A. Schiffer  
Department of Mechanical Engineering  
Khalifa University of Science and Technology  
Main Campus, P.O. Box 127788, Abu Dhabi, United Arab Emirates  
E-mail: andreas.schiffer@ku.ac.ae

S. Kumar  
James Watt School of Engineering  
University of Glasgow  
Glasgow G12 8LT, UK  
E-mail: msv.kumar@glasgow.ac.uk

 The ORCID identification number(s) for the author(s) of this article can be found under <https://doi.org/10.1002/adem.202300473>.

© 2023 Khalifa University of Science and Technology and The Authors. Advanced Engineering Materials published by Wiley-VCH GmbH. This is an open access article under the terms of the Creative Commons Attribution-NonCommercial License, which permits use, distribution and reproduction in any medium, provided the original work is properly cited and is not used for commercial purposes.

DOI: 10.1002/adem.202300473

able to design and fabricate lattice structures with specific topologies and relative densities across length scales and measure their functional properties with greater precision. This has led to a better understanding of the relationships between topology, relative density, and functional properties in lattice structures. However, further research is needed to fully understand these relationships and develop methods/tools for designing lattice structures with specific functional properties. This is an active area of research in materials engineering and holds potential for a wide range of applications in various engineering disciplines. The advent of cutting-edge manufacturing techniques like additive manufacturing (AM), or 3D printing, has made it possible to create cellular materials with intricate architectures across scales.<sup>[5,6]</sup> There are several classes of AM techniques, including fused filament fabrication (FFF),<sup>[7]</sup> stereolithography (SLA),<sup>[8]</sup> selective laser sintering (SLS),<sup>[9]</sup> directed energy deposition (DED),<sup>[10]</sup> binder jetting,<sup>[11]</sup> material jetting,<sup>[12]</sup> and laminated object manufacturing (LOM).<sup>[13]</sup> Digital light processing (DLP), a form of SLA, uses a digital light projector to cure a photosensitive resin, layer-by-layer, to create a 3D object.<sup>[14]</sup> DLP is a relatively cost-effective 3D-printing method that is known for its high-resolution and fast printing speed compared to other extant technologies like FFF. However, DLP-printed parts may need postprocessing to eliminate layer lines and/or improve the performance attributes. Additionally, DLP is limited to photocurable resins.

By combining multiple phases, lattice structures with multifunctional properties can be realized via 3D printing. Self-sensing multiphase lattice structures utilize the unique properties of nanocomposites to integrate the sensing function within the material itself, enabling real-time monitoring of the structure's response to external loads and environmental conditions. This approach allows for proactive maintenance and improved safety of critical load-bearing components, without the need for integrating additional sensors. Self-sensing behavior is often achieved by using a material's intrinsic piezoresistivity. Changes in electrical resistivity due to deformation in carbon fiber composites is an example of such behavior.<sup>[15]</sup> Due to their outstanding mechanical and electrical properties, carbon nanotubes (CNT)-based electrically conductive polymer nanocomposites have been widely used for piezoresistive sensing applications.<sup>[14,16–19]</sup> CNTs can substantially improve the electrical, mechanical, and thermal properties when incorporated as fillers in the polymer matrix.<sup>[16,20]</sup> Although a large body of literature exists on AM-enabled self-sensing composites via FFF,<sup>[16,18,21–30]</sup> only a handful of studies address this subject in the context of SLA-based techniques.<sup>[14,17,31–33]</sup> Manapat et al.<sup>[33]</sup> printed solid specimens with photopolymer resin filled with graphene oxide nanofillers using SLA and analyzed their mechanical characteristics. Recently, another study used silver nanoparticles as nanofillers in a photopolymer resin and employed SLA to print bulk specimens to investigate the effects of the nanoparticle concentration on the material's electrical, optical, and mechanical properties.<sup>[32]</sup> SLA has the potential to make high-quality products, but its production times are significantly longer than those of competing methods such as DLP. Gonzalez et al.<sup>[17]</sup> developed a photocurable resin containing uniformly dispersed CNTs and demonstrated that complicated structures, such as a 3D hexagonal lattice structure, can be successfully printed via DLP. The latter study focused on the mechanical characteristics and electrical

conductivity of the bulk materials but did not characterize the piezoresistive properties of the 3D-printed materials. Other authors examined the strain sensing and mechanical performance of DLP 3D-printed CNT-reinforced bulk specimens subject to tensile and flexural loading and demonstrated that complex parts can also be printed with good quality.<sup>[31]</sup> Mu et al.<sup>[14]</sup> utilized the DLP technique to print complex conductive structures, such as a spring and a hollow capacitor, using a photocurable resin with added nanofillers, and examined these structures for strain sensitivity and shape memory effect. Furthermore, it can also be concluded from these studies that a higher concentration of nanofillers could compromise the printability and quality of 3D-printed components. While it has been shown that SLA and DLP techniques are suitable for fabricating complex structures from nanofiller-incorporated photo-sensitive resins, information on the mechanical and self-sensing performance of SLA or DLP 3D-printed lattice structures is still lacking. The latter techniques allow the architecture and relative density of a lattice structure to be precisely controlled and tailored to achieve a wide range of mechanical and functional properties. This is desired for exploring the effects of lattice architecture and relative density on the piezoresistive self-sensing performance, which is a fundamental question that has not yet been fully addressed in the literature.

This study investigates the mechanical and strain sensing performance of 2D lattice structures processed via DLP using an electrically conductive nanocomposite resin containing a small amount (0.025 phr) of multiwalled carbon nanotubes (MWCNTs). The mechanical and piezoresistive sensing functionalities of the 3D printed lattice structures were experimentally evaluated under monotonic and cyclic tensile loading for various cell topologies (hexagonal, chiral, triangular, and reentrant) and relative densities (20%, 30%, or 40%). In addition, nonlinear finite element (FE) calculations were performed to predict the mechanical responses of the 2D lattice structures, including the progression of strut damage and failure under tensile loading conditions. The primary goal of this study is to unveil fundamental relations between lattice topology, relative density, and piezoresistive sensing performance in bend- and stretch-dominated lattices using both experimental and numerical approaches.

## 2. Experimental Section

### 2.1. Materials

The resin employed in this research is a blend of PlasClear photocurable resin (Asiga, Alexandria, Australia), diphenyl (2,4,6-trimethyl benzoyl) phosphine oxide (TPO) photoinitiator (AllPlace, Shandong, China), and tripropylene glycol diacrylate (TPGDA) (AllPlace, Shandong, China). TPGDA was used as a reactive diluent. MWCNTs were used as conductive fillers and were purchased from Applied Nanostructured Solutions LLC (Baltimore, Maryland, United States).

### 2.2. Preparation of Nanocomposite Resin

First, 2.5 phr of TPO was completely dissolved in 50 phr TPGDA via magnetic stirring for 30 min (all the concentrations were

taken by weight) followed by the addition of 0.025 phr MWCNTs. The mixture was then probe sonicated at 35 Hz for 8 min under continued magnetic stirring to uniformly disperse the MWCNTs, alternating between ON (5 s) and OFF (15 s) cycles to prevent overheating. The sonicated mixture was then added to 50 phr PlasClear followed by magnetic stirring for another 30 min. Note that the MWCNT loading in the liquid resin (0.025 phr) was sufficiently high to achieve electronic percolation in the printed samples, yet low enough to guarantee high-quality prints, as detailed in a previous study.<sup>[34]</sup> The prepared nanocomposite resin had a dynamic viscosity of 178.2 cP (measured using an SVM 3000 Stabinger Viscometer, Anton Paar, Austria) which is lower than that of the neat PlasClear resin (342 cP), thanks to the addition of the reactive diluent TPGDA.

### 2.3. DLP 3D Printing

The 2D lattice structures were fabricated using an Asiga Freeform Pro 2 DLP 3D printer (Asiga, Alexandria, Australia); the as-prepared nanocomposite resin (see Section 2.2) was used as the feedstock. The Freeform Pro2 is a UV-curing, bottom-up DLP printer that uses a 385 nm LED-based UV lamp to cure a layer of resin between the vat and the build platform by projecting an image composed of square pixels with an XY resolution of 75  $\mu\text{m}$ . Since the resin between the vat and the build platform (with a gap width of approximately 50  $\mu\text{m}$ ) is cured in a single step, the orientation of the CNTs is expected to be multidirectional in each layer.

As shown in **Figure 1**, four different unit cell topologies, namely hexagonal, chiral, triangular, and reentrant geometries were considered. The reason for choosing these four topologies

was to compare the self-sensing behavior of bend-dominated (hexagonal and chiral) and primarily stretch-dominated (triangular, reentrant) lattices (The reentrant lattice is not fully stretch-dominated due to the occurrence of bending moments on either side of the angled struts. However, these bending moments are relatively small since the angled struts are nearly vertical). Moreover, the reentrant and chiral topologies were chosen to examine the effect of auxeticity (i.e., negative Poisson's ratio) on the sensing performance of bend- and stretch-dominated lattices. All specimens consisted of a  $20 \times 8$  array of unit cells and had a constant out-of-plane thickness of 2 mm. The in-plane thickness of the struts in these lattices was varied without changing the unit cell size to obtain structures with three different relative densities ( $\rho = 20\%, 30\%, 40\%$ ). Note that the struts in the two rows of unit cells at the top and bottom of the specimen were thickened to facilitate gripping of the specimen during mechanical testing. The dimensions for each type of unit cell are shown in Figure S1, Supporting Information, and are listed in Table S1, Supporting Information, for each specimen. The SolidWorks software (version 2020, Dassault Systèmes, SolidWorks Corp., USA) was used to create CAD files for all specimen geometries, and these were then sliced using the Asiga Composer software (version 1.1.9). The slices were 50  $\mu\text{m}$  thick, the exposure time was set to 7 s for each layer, and the light intensity was 5.20  $\text{mW cm}^{-2}$  for all samples (unless otherwise stated).

### 2.4. Piezoresistive and Mechanical Testing

The mechanical and piezoresistive sensing performance of the 3D-printed lattice structures were experimentally evaluated

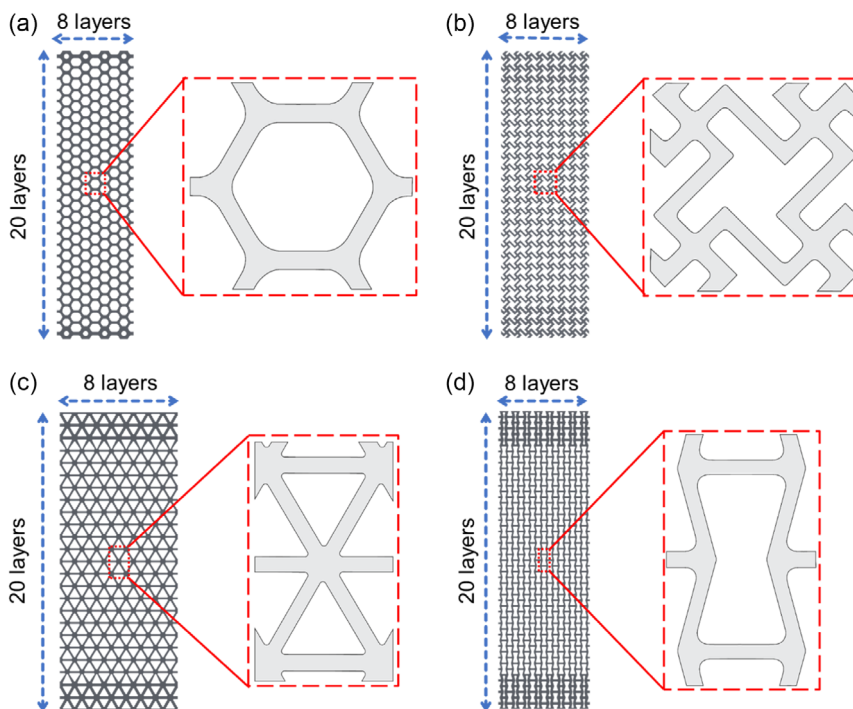


**Figure 1.** 2D lattice structures with a) hexagonal ( $90.8 \times 24.4 \text{ mm}^2$ ), b) chiral ( $91.4 \times 28.4 \text{ mm}^2$ ), c) triangular ( $80.7 \times 28.7 \text{ mm}^2$ ), and d) reentrant ( $91.6 \times 28.4 \text{ mm}^2$ ) unit cell geometries; the images correspond to 40% relative density.

under monotonic and cyclic loading conditions, as detailed in the following.

#### 2.4.1. Monotonic Tensile Tests

A Zwick/Roell universal testing machine (UTM, model Z005) was used to conduct tensile tests on the 3D-printed samples. The specimens were placed between the wedge action grips of the UTM and clamped at both ends over a region comprising two unit cells, ensuring a gauge section of  $16 \times 8$  unit cells. Displacement-controlled tensile tests were conducted until failure at a cross-head speed of  $2.5 \text{ mm min}^{-1}$ , and the force,  $F$ , induced in the specimen was measured using a 2.5 kN load cell. The force readings were then converted into engineering stress,  $\sigma = F/A_0$ , where  $A_0$  is the initial cross-sectional area of the entire gauge section (i.e., lattice voids included). The crosshead displacement recorded by the UTM was assumed to be equal to the elongation of the specimen,  $\Delta L$ , and was used to calculate the applied strain,  $\varepsilon = \Delta L/L_0$ , where  $L_0$  is the gauge length of the specimen. It should be noted that the crosshead displacement can differ from the sample's elongation due to grip slippage and the deformation induced in the loading train. However, the latter effects are expected to be negligible, due to the relatively low modulus and strength of the samples tested herein. For comparison purposes, some samples were also tested on another UTM (Instron, 50 kN load capacity), and the results obtained from both machines were found to be in close agreement. In each test, a Tektronix 6.5-digit DMM 4050 multimeter (range: 0.01–1000 M $\Omega$ ) was used to measure the electrical resistance change,  $\Delta R = R - R_0$ , in situ, where  $R$  is the actual resistance of the test specimen at strain  $\varepsilon > 0$ , and  $R_0$  is the no-load resistance, corresponding to  $\varepsilon = 0$ . It is important to take note that the probes of the multimeter were connected to a copper tape placed between the grips of the UTM and the specimen. The copper tape was extended throughout the width of the samples and was insulated from the loading train of the UTM using strong insulating tape. The multimeter readings were then synchronized with the stress–strain data recorded by the UTM using a computer. The obtained  $\Delta R/R_0$  versus  $\varepsilon$  data was used to evaluate the gauge factor,  $k$ , which quantifies the average sensitivity of a piezoresistive material and is defined as

$$k = \frac{\Delta(\Delta R/R_0)}{\Delta\varepsilon} \quad (1)$$

where  $\Delta\varepsilon$  is the strain interval over which  $\Delta R/R_0$  was measured. To verify the repeatability of the measurements, at least three tests were carried out in succession on virgin specimens for each type of specimen.

#### 2.4.2. Repeated Cyclic Tests

The cyclic responses of the 3D-printed lattices were tested under repeated cyclic strains utilizing the same experimental setup as in the monotonic tensile tests described above. In these tests, the samples were loaded in tension up to  $\varepsilon = 1\%$ , and were then promptly unloaded to  $\varepsilon = 0.5\%$ . The latter load–unload cycles were repeated to obtain a total of 10 or 100 cycles. Note that the strain amplitudes were kept deliberately low to guarantee that the response would be predominately elastic. The change in

electrical resistance was recorded, as described above, to examine the stability of the strain-sensing functionality under repeated low-amplitude strain cycles.

#### 2.5. Microcomputed Tomography ( $\mu$ CT)

X-ray microcomputed tomography ( $\mu$ CT) analysis was performed to examine the microscale struts of the 3D-printed lattice structures and identify the presence of manufacturing defects (e.g., voids, delaminations, etc.) using a Phoenix nanom M nano-CT 3D scanner (GE Sensing & Inspection Technologies GmbH). Hexagonal, chiral, triangular, and reentrant lattice structures with 40% relative density were scanned at a resolution of 10  $\mu\text{m}$ . Imaging was accomplished using a microfocus X-ray beam and a flat panel detector. The acceleration voltage was set at 90 keV, and the beam current was set at 50 A.

### 3. Numerical Modeling

Nonlinear finite element calculations were performed in ABAQUS/Explicit (version 2022) to provide further insight into the deformation and failure modes observed in the 2D nanocomposite lattice structures during tensile loading. The 3D CAD models were imported in ABAQUS and meshed using 8-node brick elements (C3D8R in ABAQUS). Note that only one-quarter of the specimens' gauge sections were modeled due to symmetry. The element size was approximately 0.1 mm which resulted in 210 640, 295 520, and 389 180 elements for structures with 20%, 30%, and 40% relative density (values apply to the hexagonal lattice), respectively. Examples of the generated FE meshes are shown in Figure S4–S7, Supporting Information. The constitutive response of the nanocomposite resin was modeled using isotropic linear elasticity combined with a Drucker–Prager (DP) plasticity model to capture pressure-dependent yielding of the polymer; the occurrence of damage and failure in the material was accounted for by including the Ductile Damage model in the constitutive description. A similar constitutive model was used in a recent study on dynamic crushing of DLP 3D printed honeycombs<sup>[35]</sup> made from the same type of resin, but without the added CNTs. In the present study, the original model parameters (as used in ref. [35]) were adjusted to capture the stress vs. strain responses obtained from a series of uniaxial tension and compression tests (shown in Figure S3, Supporting Information) performed on the 3D printed MWCNT-filled resin with 0.025 phr nanofiller loading. A summary of the constitutive parameters is presented in **Table 1**. Since DLP can produce structures with varying crosslinking density, their mechanical properties can vary significantly from one specimen to another. Hence, the constitutive model parameters (see Table 1) were based on the average mechanical properties (i.e., Young's modulus, yield stress, ultimate strength, and failure strain) obtained from a series of 4–6 tests performed on identical virgin specimens. Note that the flow curve was specified based on the measured tensile stress versus strain data (see Figure S3a, Supporting Information). To prevent the dilation of the polymer during plastic straining, we made use of a nonassociated flow rule. This flow rule was selected with a dilation angle that was set very close to zero.<sup>[35]</sup> In addition, the DP model was designed with a friction angle of



**Table 1.** Input parameters for the constitutive model used in the FE calculations, corresponding to the average properties of the 3D-printed nanocomposite resin with 0.025 phr CNT loading.

Description	Values	
Physical properties		
Mass density	1,180 kg m <sup>-3</sup>	
Elasticity		
Young's modulus	491 MPa	
Poisson's ratio	0.47	
Drucker–Prager plasticity		
Angle of friction	24	
Flow stress ratio	1	
Dilation angle	1	
Ductile damage		
Fracture (true) strain	0.65	0.145
Stress triaxiality	−0.33	0.33
Fracture energy	80 N m <sup>-2</sup>	

$\beta = 24^\circ$ . This angle was chosen specifically to match the pressure-sensitive yielding of the polymer (i.e., the discrepancies in the measured tensile and compressive yield stresses, see Table S2, Supporting Information). Further details on the calibration

procedure can be found in the literature.<sup>[35]</sup> Uniaxial tensile loading was induced by displacing the top edge of the specimen in the vertical direction (i.e., parallel to the Y-direction in Figure S4–S7, Supporting Information) until the structure failed in tension. A dummy node tied to the nodes on the top edge was used to control the deformation of the specimen and extract the reaction force predicted by the FE model. Based on the latter data, the effective stress vs. strain response of the lattice structure was calculated and compared to the measurements.

## 4. Results and Discussion

### 4.1. Microstructure Analysis

The  $\mu$ CT images of the chiral, reentrant, hexagonal, and triangular lattice structures are shown in Figure 2a–d, respectively. The zoomed images show cross-sections of the scanned lattices in selected regions. In these images, the individual layers of the DLP print are clearly visible on the lateral surfaces of the lattice structures. The 3D-printed structures closely resemble the geometries of their respective CAD files, suggesting that the XY resolution of the 3D printer (75  $\mu$ m) was sufficient to capture the smallest features of the unit cell designs. Moreover, the images reveal that the structures are free of internal defects (>10  $\mu$ m), showing no signs of embedded voids or delamination, confirming the excellent printability of the prepared nanocomposite resin.

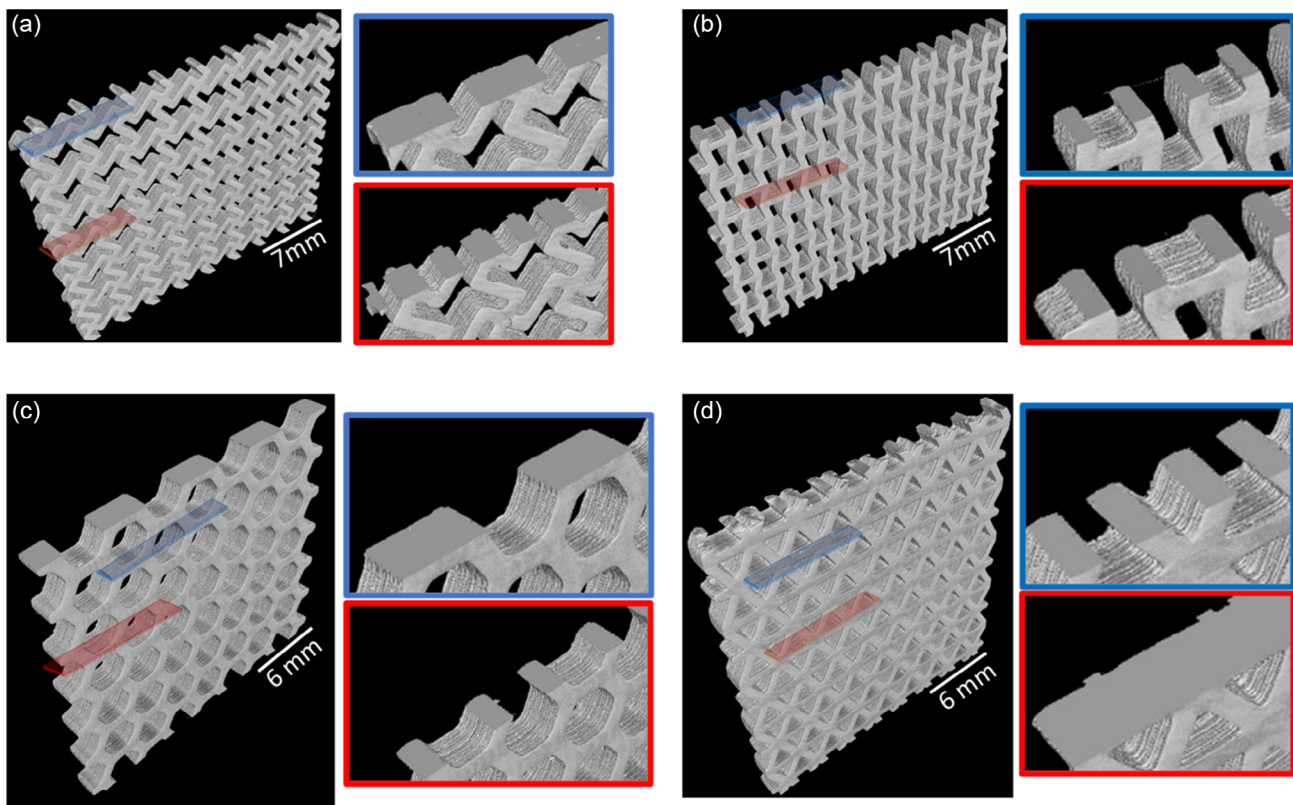


**Figure 2.** Micro-CT scans of a) chiral, b) reentrant, c) hexagonal, and d) triangular lattice structures (all with 40% relative density), along with zoomed cross-sectional scans at two different locations (red and blue).

## 4.2. Mechanical and Piezoresistive Responses Under Monotonic Tensile Loading

The measured nominal stress versus strain curves of the 2D lattices with four different cell geometries are presented in **Figure 3a–d**, along with the corresponding FE predictions. Each of the figures includes measurements and predictions for three different relative densities (20, 30, and 40%). Numerical values of the predicted and measured ultimate strengths and elastic moduli are summarized in Table S3, Supporting Information. For all cell topologies, an increase in modulus and ultimate strength is observed with increasing relative density, as expected, and this was found to be slightly more pronounced for the bend-dominated structures (hexagonal and chiral, see **Figure 3a,b**) than for the stretch-dominated ones (triangular and reentrant, see **Figure 3c,d**). Most of the 2D lattices failed in a brittle manner, due to the limited ductility of the parent material (see supporting **Figure S3a**, Supporting Information). At lower relative densities (i.e., 20%), however, a distinct softening response was observed for most lattice geometries as a result of incremental failure of the thin struts. The 3D printing process introduces random variations in struts thickness at a certain length scale which have a larger effect on strut failure if they are thin, resulting in larger spatial variations of failure strain within the lattice structure and thus promoting incremental failure. For the two bend-dominated lattices (see **Figure 3a,b**), the failure strain decreases with increasing relative density, which was not observed for the stretch-dominated structures (see **Figure 3c,d**). When the struts of the lattice undergo bending, the maximum stresses induced in the struts increase with increasing strut thickness and this causes failure at lower macroscopic strains, (provided that the ductility of the parent material is limited, which is the case here). Hence, the decrease in strain tolerance with increasing relative density, as observed for the hexagonal and chiral lattice, can be seen as an indication of bend-dominated behavior. Among the two stretch-dominated lattices (triangular and reentrant, see **Figure 3c,d**), the reentrant structures fail at a lower macroscopic strain than the triangular lattice, since the struts of the reentrant lattice undergo bending stresses because of their angled configuration. Although these bending stresses are smaller in magnitude than those induced by stretching of the struts (since the struts are nearly vertical), they raise the surface stresses near the nodal points and therefore limit the ductility of the lattice. As shown in **Figure 3a–d**, the FE predictions capture the measured stress–strain responses of all types of lattice structures with good accuracy. While this gives confidence in the predictive capabilities of the developed FE models, it remains to be shown whether they can capture the deformation and failure modes observed in the experiments, which is discussed next.

In **Figure 4**, we present a sequence of photographs of the deformed specimens (all with 40% relative density) at different levels of strain along with the corresponding contour plots of the von Mises stress, as predicted by the FE model. Note that the contour plots only show one quarter of the specimens' gauge sections, as indicated by the dashed orange boxes in the photographs. As seen from **Figure 4a,c,d**, the hexagonal, triangular, and reentrant structures started to fail by fracture of lattice struts near the edge of the specimen's gauge section, giving rise to the propagation of a macroscopic crack along the weakest path. The corresponding FE

predictions were able to capture the observed failure modes with good accuracy, aside from the fact that initiation of fracture occurred closer to the top edge in the FE simulations, while in the experiments, the cracks propagated closer to the specimen's mid-plane. Since the FE predictions were based on ideal geometric models and do not account for any imperfections introduced during 3D printing process, the predicted fracture paths are expected to deviate from those observed in the experiments. In the experiments performed on the chiral lattices, fracture occurred at the end of the specimen's gauge section (i.e., close to the grips) in a plane perpendicular to the loading direction, as shown in **Figure 4b**. The unit cells of the chiral lattice structure rotate and distort during the tensile test, causing stress concentrations at the end of the specimen's gauge section near the free edge, as confirmed by the FE predictions (see **Figure S4**, Supporting Information). Note that such stress concentrations were observed to a lesser extent in the predicted stress fields of the reentrant, hexagonal, and triangular lattices (see **Figure S5–S7**, Supporting Information).

We now proceed to examine the influence of the unit cell geometry and relative density on the piezoresistive responses of the 3D printed lattices which were measured in situ during the uniaxial tensile tests. The addition of 0.025 phr CNTs to the resin was sufficient to achieve electric percolation in the 3D-printed lattice structures, reporting an average isotropic conductivity in the range of  $3.3 \times 10^{-5}$ – $6.6 \times 10^{-7}$  S cm<sup>-1</sup>, depending on the unit cell geometry and relative density. When a tensile load is applied on the structure, the CNTs in the percolating network move apart, resulting in an increase in the electrical resistance of the structure which is typically quantified by  $\Delta R/R_0$  where  $\Delta R = R - R_0$ , with  $R_0$  and  $R$  denoting the resistance at zero and nonzero strain, respectively.<sup>[15,22,36,37]</sup>

The normalized resistance changes  $\Delta R/R_0$  measured for the hexagonal, chiral, triangular, and reentrant lattice structures are plotted against the applied strain in **Figure 3e–h**, respectively; in each of these figures, measurements are included for lattices with 20, 30, and 40% relative density. It can be seen that the piezoresistive responses of all types of structures are nearly linear irrespective of their relative density. The fluctuations observed in the  $\Delta R/R_0$  signals are attributed to changes in the morphology of the conductive network within the cell walls with increasing deformation, causing conductive channels in the network to be formed and reformed incrementally. While the piezoresistive sensitivity is seen to increase with increasing relative density for the bend-dominated hexagonal and chiral structure (**Figure 3e,f**), the relative density has no significant effect on the piezoresistive response of the stretch-dominated triangular and reentrant structures (**Figure 3g,h**). When a stretch-dominated structure is subject to a macroscopic tensile strain  $\epsilon$ , the percolating networks of nanofillers in all load-bearing struts are subject to uniaxial straining (i.e., uniform strain fields), hence yielding a piezoresistive response insensitive to the thickness of the lattice struts. In contrast, at a given macroscopic strain  $\epsilon$ , the percolating network in bend-dominated structures experiences higher strains if the struts are thicker, effectively increasing the sensitivity of the network resistance to the applied macroscopic strain. It is also worth noting that some of the simulations in **Figure 3** are undershooting the measured stress versus strain responses. This could be

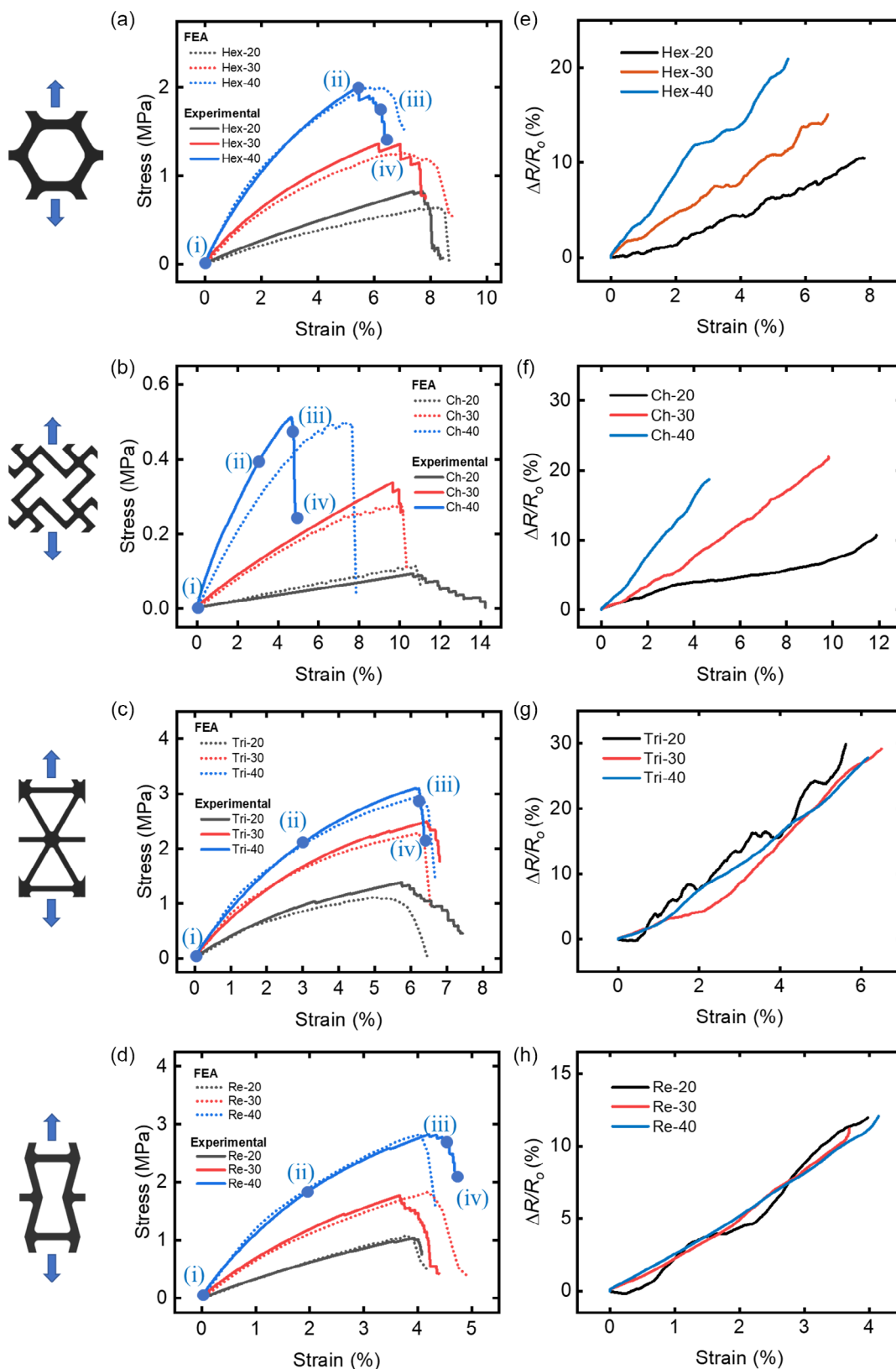


**Figure 3.** Stress–strain a–d) and piezoresistive e–h) responses of hexagonal, chiral, triangular, and reentrant lattice structures with 20%, 30%, and 40% relative density.



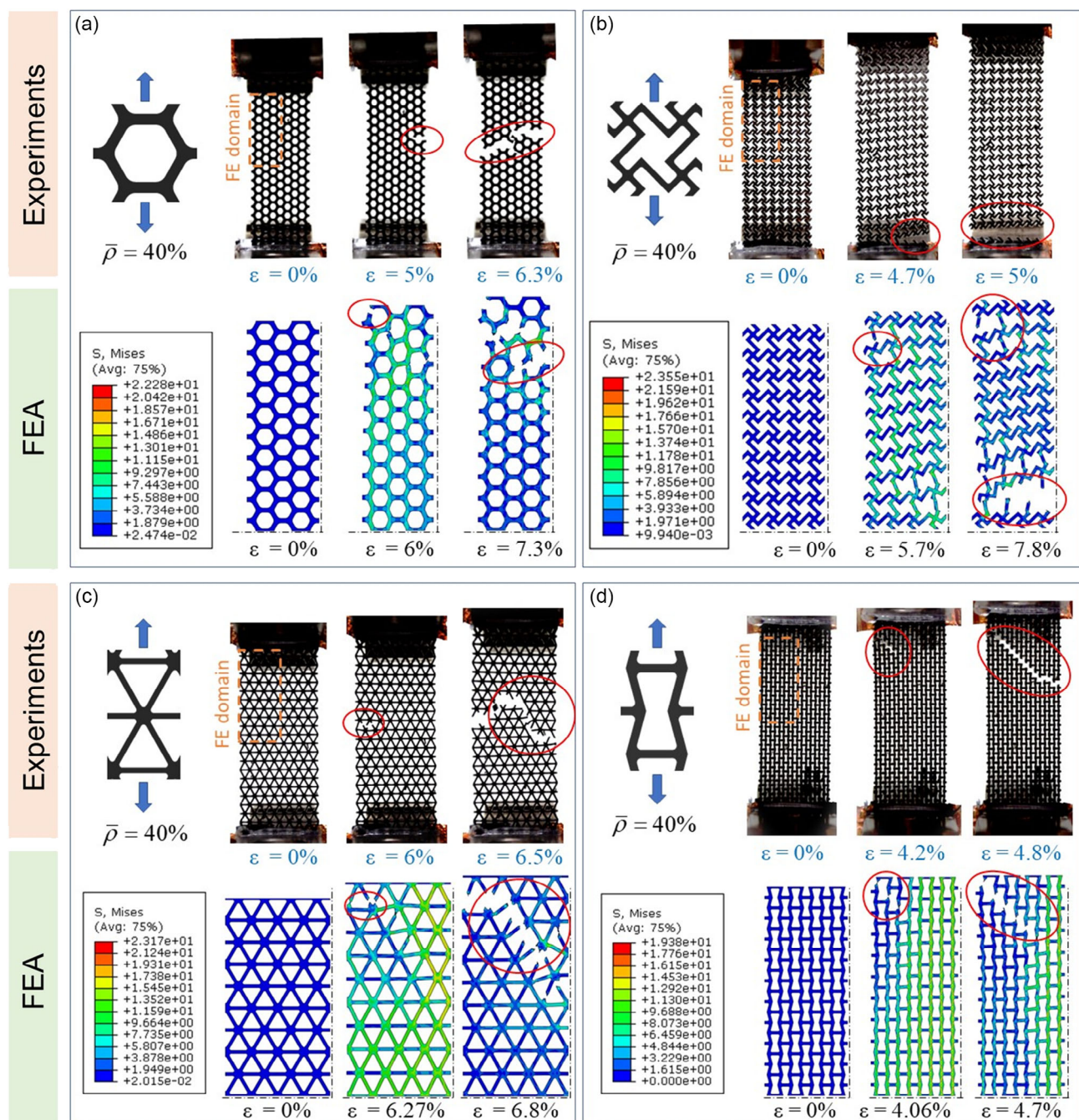


**Figure 4.** Maps (from experiments and FEA) depicting the deformation and failure behavior of a) hexagonal, b) chiral, c) triangular, and d) reentrant lattice structures with 40% relative density.

due to the intrinsic scatter in the mechanical properties of DLP 3D-printed structures, resulting from variations in the cross-linking density of the photo-cured resin. While the cross-linking density in a DLP 3D-printed object primarily depends on the process parameters (e.g., slice thickness, exposure time, light intensity, etc.), which were kept constant for all samples printed in this study, the cross-linking density is also affected by the presence of oxygen which can inhibit photopolymerization and lead to size effects.<sup>[38,39]</sup>

### 4.3. Effect of Relative Density on the Mechanical and Electrical Properties

The modulus ( $E$ ) and strength ( $\sigma^*$ ) of lattice structures scale with relative density ( $\bar{\rho}$ ) in the form of a power law which is widely known as the Gibson–Ashby model<sup>[4]</sup>

$$E/E_s = A\bar{\rho}^n, \sigma^*/\sigma_s^* = B\bar{\rho}^m \quad (2)$$



where  $A$  and  $B$  are proportionality constants,  $n$  and  $m$  are the scaling exponents, and  $\sigma_s^*$  and  $E_s$  are the strength and Young's modulus of the constituent material, respectively. The scaling exponents  $n$  and  $m$  can be used to categorize lightweight cellular structures according to the nature of their fundamental deformation mode (bending or stretch-dominated).<sup>[40]</sup> When  $n = m \approx 1$ , the 2D or 3D lattice structure deforms by elongation or shortening of its members under external loading, thus yielding stretch-dominated behavior. For bend-dominated structures, the latter exponents are typically larger resulting in a stronger coupling between the mechanical properties and relative density. Specifically, for bend-dominated 2D lattices, typical values for the scaling exponents are  $n \approx 3$  and  $m \approx 2$  (for bend-dominated 3D lattices,  $n \approx 2$  and  $m \approx 1.5$ ).

The predicted values of normalized modulus,  $\bar{E} = E/E_s$ , and strength,  $\bar{\sigma} = \sigma^*/\sigma_s^*$ , of the four types of lattice structures are

plotted as functions of relative density,  $\bar{\rho}$ , in **Figure 5a,b**, respectively. Also included in these figures are the least-square fits of the Gibson–Ashby scaling law (Equation (2)) to the predicted data, with the obtained fitting parameters  $A$ ,  $B$ ,  $m$ , and  $n$  listed in Table S4, Supporting Information. It is clear from Figure 5a, b, that the Gibson–Ashby model gives a very good description of the predicted data with scaling exponents of  $\{n,m\} = \{2.6,1.6\}$  for the hexagonal and  $\{3.2,2.2\}$  for the chiral lattices, confirming their bend-dominated response. For the stretch-dominated triangular and reentrant lattices, the latter exponents were significantly lower, as expected, reporting  $\{n,m\} = \{1.4,1.4\}$  and  $\{1.9,1.5\}$ , respectively. Similar trends were observed for the measured  $\bar{E}$  versus  $\bar{\rho}$  and  $\bar{\sigma}$  versus  $\bar{\rho}$  plots presented in Figure 5c,d, respectively, which were also found to closely follow the Gibson–Ashby scaling equation, as expected. Both the measurements and predictions show that the triangular lattice

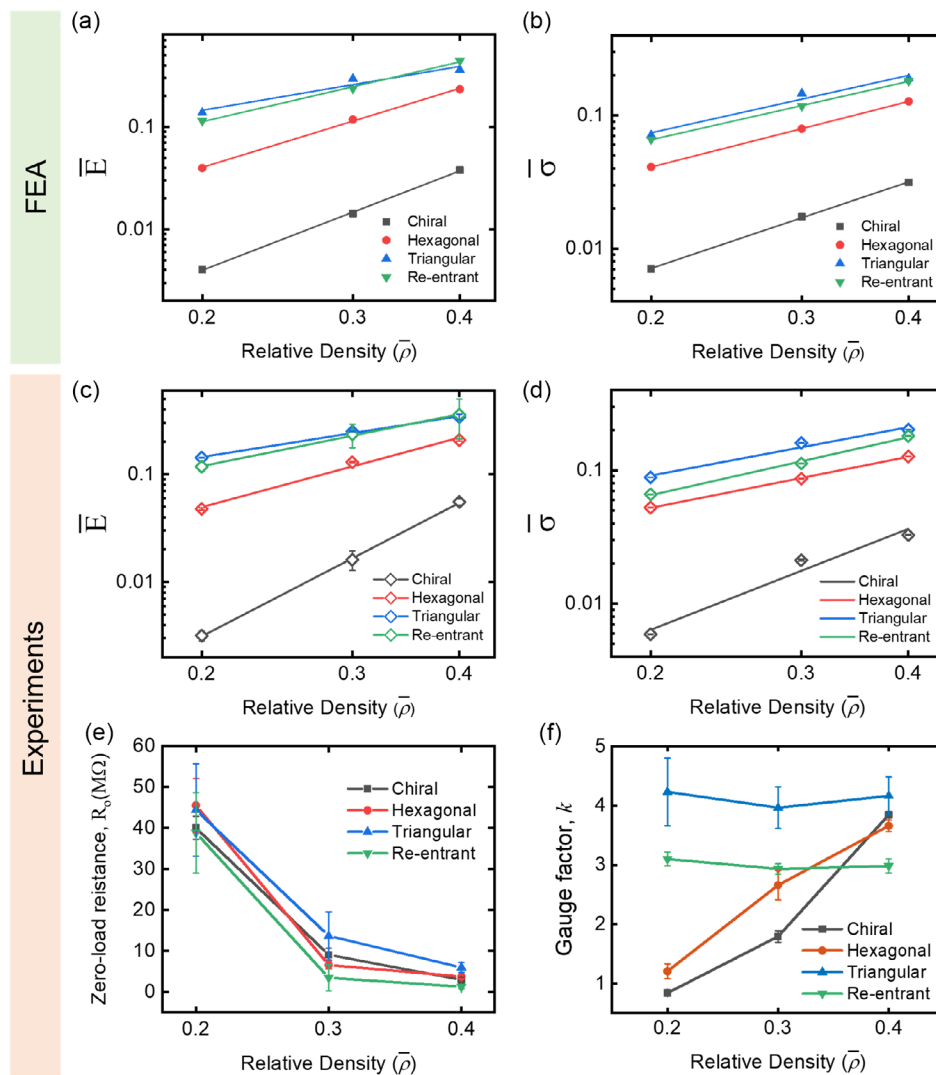


**Figure 5.** a) Normalized elastic modulus and b) normalized tensile strength obtained via FEA, c) normalized elastic modulus, and d) normalized tensile strength obtained experimentally, e) effect of relative density on zero-load resistance, and f) the gauge factors of chiral, hexagonal, triangular, and reentrant lattice structures with three different relative densities (20%, 30%, and 40%).

possessed the highest strength and modulus over a wide  $\bar{\rho}$  range, with the reentrant, hexagonal, and chiral lattices following in order.

Figure 5e shows that the zero load resistance,  $R_0$ , follows an inverse relationship with the relative density for all types of lattice structures considered. As the thickness of the lattice struts (and hence the relative density) increases, additional conductive channels are established in the percolating network, resulting in reduced electrical resistance.

Figure 5f presents gauge factor versus relative density plots for the four different lattice structures considered here. Note that these gauge factors were evaluated within a strain range of  $0\% \leq \epsilon \leq 4\%$ . It can be seen that an increase in relative density causes the gauge factors of the bend-dominated hexagonal and chiral structures to increase, while the piezoresistivity of the stretch-dominated triangular and reentrant structures was found to be nearly insensitive to the relative density, as discussed in Section 4.2. Specifically, we observed an increase of  $\approx 550\%$

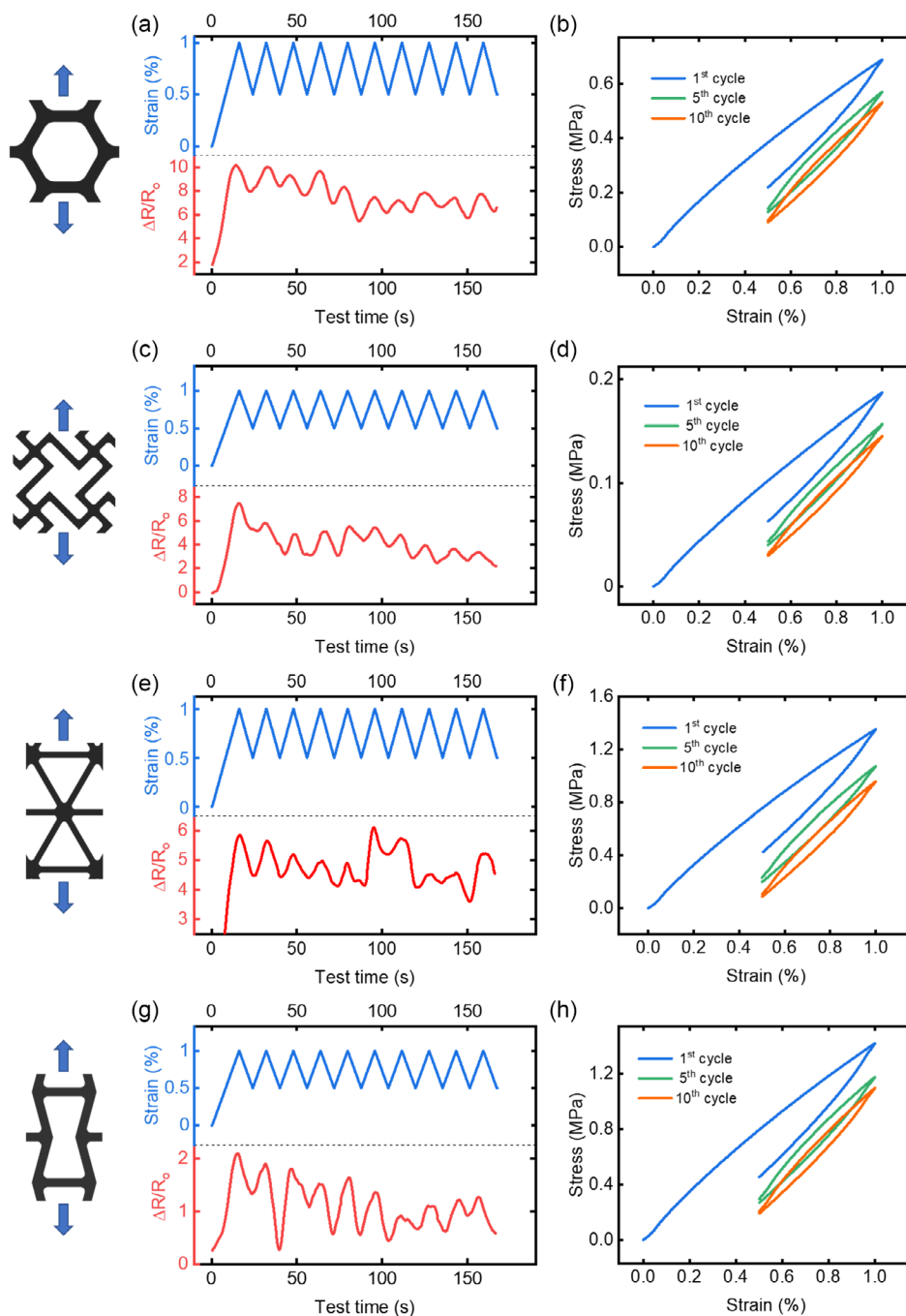


**Figure 6.** Piezoresistive and mechanical responses of a,b) hexagonal, c,d) chiral, e,f) triangular, and g,h) reentrant lattice structures (all with 30% relative density) subject to 10 strain-controlled tensile load cycles.

and  $\approx 300\%$  in gauge factor for chiral and hexagonal structures, respectively, when increasing the relative density from 20% to 40%. Among the four types of lattice structures, the triangular lattices achieved the highest gauge factors ( $k \approx 4.1$ ) over the entire  $\bar{\rho}$  range considered, which is attributed to their stretch-dominated behavior, causing nearly uniform straining of the percolating network in the lattice struts. For  $\bar{\rho} \leq 0.3$ , the gauge factors vary with the cell topology in a manner similar to that observed for the modulus and strength (see Figure 5a–d). At higher relative densities,  $\bar{\rho} > 0.3$ , the  $k$  values of all types of lattice structures start to approach a common level. This is not unexpected because with increasing  $\bar{\rho}$ , the piezoresistivity of the material in the struts becomes less dominant, as more material volume is shifted to the lattice nodes, leading to a common saturation piezoresistive behavior for all structures. It is worth noting that the mechanical and electrical properties of cellular structures can change if the relative densities of the printed parts differ from the CAD model. Therefore, the relative densities of the lattice structures were calculated using the measured weights of the samples and were found to closely match the intended relative densities.

#### 4.4. Mechanical and Piezoresistive Responses Under Strain-Controlled Cyclic Loading

Figure 6 reports the mechanical and piezoresistive responses of hexagonal (Figure 6a,b), chiral (Figure 6c,d), triangular (Figure 6e,f), and reentrant (Figure 6g,h) lattice structures subject to 10 repeated strain cycles. The strain amplitudes were kept deliberately lower than  $\varepsilon = 1\%$  to guarantee that the response would be predominately elastic. The first column of graphs in Figure 6 shows time histories of the measured  $\Delta R/R_0$  and applied strain data, while the second column presents the corresponding stress vs. strain responses. As seen from Figure 6b,d,f, h, the peak stress was found to decline with increasing number

of cycles which is attributed to stress relaxation processes in the viscoelastic polymer matrix.<sup>[41]</sup> Since the elastic moduli of the triangular and reentrant lattices were higher than those of the hexagonal and chiral ones (see Figure 5c), the peak stresses recorded during the cyclic tests of the former lattices were higher (see Figure 6). Moreover, wide hysteresis loops in the stress-strain response are observed during the first load cycle for all types of lattice structures, but these become narrower as the number of cycles increases, indicating that the energy dissipated by viscoelastic damping declined during the test. In addition, it is observed from Figure 6a,c,e,g that the maximum and minimum  $\Delta R/R_0$  values gradually decreased as the number of cycles increased which can be attributed to the viscoelastic nature of the polymer matrix separating the conductive CNT nanofillers. Some chain segments in the polymer network relax faster than others, preventing some of the CNTs from returning to their original position upon unloading. Hence, the morphology of the percolating network continuously changes during cyclic loading since there is not enough time for the polymer matrix to return to a fully relaxed state after the load is reversed. It is also seen from Figure 6 that the stress and  $\Delta R/R_0$  responses of all types of lattice structures show similar declining trends, which is expected since these lattice structures were 3D printed from the same base material.

To examine the long-term stability of the strain-sensing performance, an additional test was performed in which the triangular lattice (30% relative density) was subject to 100 strain cycles in the range of  $0.5 \leq \varepsilon \leq 1.0\%$ . Since such test is very time-consuming, only the triangular lattice was selected for this test due to its superior mechanical characteristics. The measured time histories of stress and  $\Delta R/R_0$  are plotted in Figure 7a for cycles 1–10, 45–55, and 90–100. The graph shows that the peak stresses decrease significantly over the first 10 load cycles, in line with the results of Figure 6, but then reach a stationary value of  $\approx 0.4$  MPa after around 50 load cycles. This is also evident from

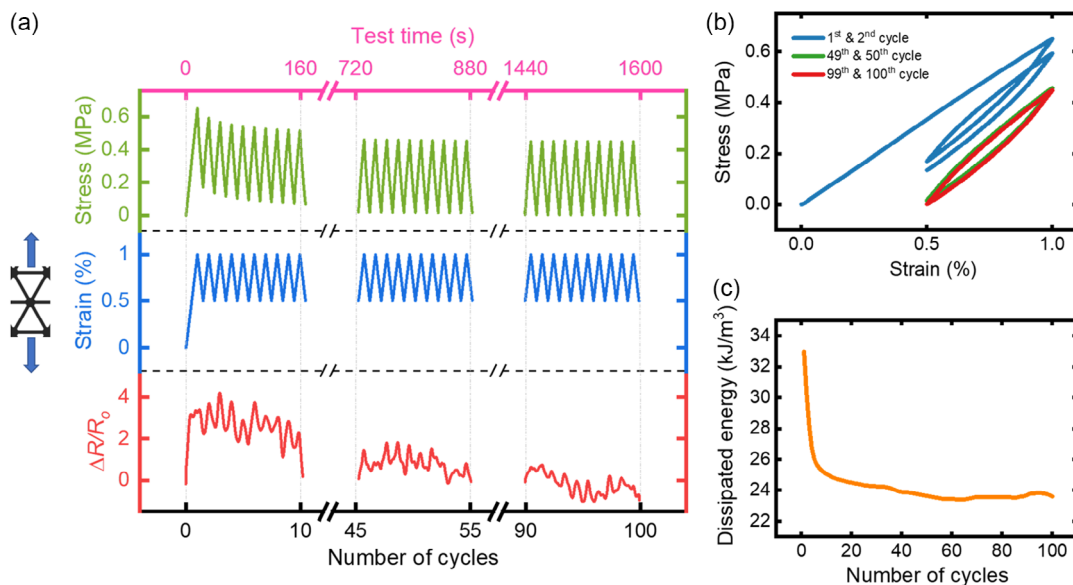


**Figure 7.** a) Piezoresistive response, b) hysteresis response, and c) dissipated energy of triangular lattice structure upto 100 cycles under quasi-static tensile cyclic loading.



the stress-strain response shown in Figure 7b where the hysteresis loops are nearly identical for the 50<sup>th</sup> and 100<sup>th</sup> load cycle. This indicates that the energy dissipated per load cycle is nearly constant in the second half of the test period, and the data presented in Figure 7c confirm this. Such transient effects in the mechanical response can be attributed to the stress relaxation associated with the nonzero mean stress, which approaches asymptotically a limit of  $\approx 0.2$  MPa after 40–50 cycles (or, a duration of 800 s). Although the mechanical response stabilizes in the first period of the test, this does not directly translate into a stable piezoresistive response, as seen from Figure 7a, where the  $\Delta R/R_0$  signal continues to decline between the 50<sup>th</sup> and 100<sup>th</sup> cycle. Since viscoelastic damping persists beyond the 50<sup>th</sup> cycles (as seen from Figure 7b,c), the morphology of the percolating network continues to change over time, since the polymer matrix supporting the percolating network is unable to return to a fully relaxed state upon unloading. Although such time-dependent piezoresistive behavior would make it challenging to determine the actual strain level under repeated load–unload cycles, these nanocomposites can still be useful for a range of applications in structural health monitoring, such as the detection of vibrations, overloads, or impacts during service.

## 5. Conclusion

In this study, the DLP technique was utilized to additively manufacture multiphase 2D lattice structures with integrated strain sensing functionality, achieved by dispersing a small amount of CNTs (0.025 phr) in the photocurable acrylic resin. The lattice structures with different cell topologies (hexagonal, chiral, triangular, or reentrant) and relative densities (20%, 30%, or 40%), were realized and their mechanical and piezoresistive self-sensing characteristics under both monotonic tensile and repeated cyclic loading were examined. In addition, detailed nonlinear finite element studies were conducted accounting for the pressure-dependent yielding of the nanocomposite to predict the stress–strain responses of the 2D lattice structures, including the progression of strut failure during loading.

Both the measurements and predictions showed that the triangular lattice possessed the highest strength and modulus over a wide relative density range, with the reentrant, hexagonal, and chiral lattices following in order. A stronger coupling between strength/modulus and relative density was reported for the hexagonal and chiral lattices due to their more pronounced bend-dominated behavior. In general, the scaling between the measured strength/modulus and relative density was well described by the Gibson–Ashby model for all cell topologies considered. The FE predictions were found in good agreement with the measured stress versus strain curves, and were able to capture the observed failure behavior with good accuracy.

The measured piezoresistive responses showed that the gauge factor of reentrant and triangular lattices were nearly insensitive to changes in the relative density which is indeed a desirable attribute for a strain sensor. In contrast, the gauge factors of the hexagonal and chiral lattice structures rose by 300% and 500%, respectively, with an increase in relative density from 20 to 40%. The stronger coupling between piezoresistivity and relative density in the latter lattice structures was attributed to their

pronounced bend-dominated response. At constant macroscopic strain, the peak strains in the struts of bend-dominated lattices increase with increasing relative density, thus causing more pronounced changes in the morphology of the conductive network within the cell walls. The higher sensitivity of these topologies suggests that they can be useful as lightweight smart structures where in situ structural health monitoring is important. Under cyclic loading with constant strain amplitudes, the electrical resistance of the 2D lattice structures was found to decline over time due to phase-lagged viscoelastic deformation of the polymer matrix which prevented the embedded CNTs from immediately returning to their original configuration upon unloading.

The results show that the self-sensing performance of 3D-printed CNT/polymer lattice structures can be tuned by controlling the relative density and cell topology (hexagonal, chiral, triangular, or reentrant). The findings of the study provide valuable insights into the coupling between sensing performance, lattice topology and relative density, and offer useful guidelines for the design of cellular strain sensors or self-sensing lightweight structures. Since DLP enables precise control of the material architecture, it is anticipated that this technology will also be useful to discover fundamental topology–property relations in other fields, such as energy storage and conversion.

## Supporting Information

Supporting Information is available from the Wiley Online Library or from the author.

## Acknowledgements

The authors are grateful for the financial support provided by Khalifa University through the Competitive Internal Research Award (CIRA) 2018 (grant no. CIRA-2018-128). This study was partially funded by ASPIRE, the technology program management pillar of Abu Dhabi's Advanced Technology Research Council (ATRC), via the ASPIRE Award for Research Excellence (grant no. AARE19-148).

## Conflict of Interest

The authors declare no conflict of interest.

## Data Availability Statement

The data that support the findings of this study are available from the corresponding author upon reasonable request.

## Keywords

3D printing, additive manufacturing, nanocomposite, photocurable resin, strain sensing

Received: April 5, 2023

Revised: June 28, 2023

Published online:

- [1] M. F. Ashby, *Materials Selection in Mechanical Design*, Butterworth-Heinemann, Burlington, MA **2011**, p. 646.
- [2] U. G. K. Wegst, H. Bai, E. Saiz, A. P. Tomsia, R. O. Ritchie, *Nat. Mater.* **2015**, *14*, 23.
- [3] M. Scheffler, P. Colombo, *Cellular Ceramics: Structure, Manufacturing, Properties and Applications*, WILEY-VCH Verlag GmbH & Co. KGaA, Weinheim **2005**, p. 645, <https://www.wiley.com/en-ae/Cellular+Ceramics%3A+Structure%2C+Manufacturing%2C+Properties+and+Applications-p-9783527313204> (accessed: January 2023).
- [4] L. J. Gibson, M. F. Ashby, *Cellular Solids: Structure and Properties*, 2nd ed., Cambridge University Press, Cambridge **1997**, pp. 1–510, <https://doi.org/10.1017/CBO9781139878326>.
- [5] L. R. Meza, A. J. Zelhofer, N. Clarke, A. J. Mateos, D. M. Kochmann, J. R. Greer, *Proc. Natl. Acad. Sci. U. S. A.* **2015**, *112*, 11502.
- [6] A. Vyatskikh, S. Delalande, A. Kudo, X. Zhang, C. M. Portela, J. R. Greer, *Nat. Commun.* **2018**, *9*, 593.
- [7] V. Mazzanti, L. Malagutti, F. Mollica, *Polymers* **2019**, *11*, 1094.
- [8] J. Z. Manapat, Q. Chen, P. Ye, R. C. Advincula, *Macromol. Mater. Eng.* **2017**, *302*, 1600553.
- [9] N. A. Charoo, S. F. Barakh Ali, E. M. Mohamed, M. A. Kuttolamadom, T. Ozkan, M. A. Khan, Z. Rahman, *Drug Dev. Ind. Pharm.* **2020**, *46*, 869.
- [10] D. G. Ahn, *Int. J. Precis. Eng. Manuf. Green Technol.* **2021**, *8*, 703.
- [11] A. Mostafaei, A. M. Elliott, J. E. Barnes, F. Li, W. Tan, C. L. Cramer, P. Nandwana, M. Chmielus, *Prog. Mater. Sci.* **2021**, *119*, 100707.
- [12] O. Gülcan, K. Günaydin, A. Tamer, *Polymers* **2021**, *13*, 2829.
- [13] B. Bhushan, M. Caspers, *Microsyst. Technol.* **2017**, *23*, 1117.
- [14] Q. Mu, L. Wang, C. K. Dunn, X. Kuang, F. Duan, Z. Zhang, H. J. Qi, T. Wang, *Addit. Manuf.* **2017**, *18*, 74.
- [15] S. Wang, D. D. L. Chung, J. H. Chung, *J. Mater. Sci.* **2005**, *40*, 6463.
- [16] J. M. Wernik, S. A. Meguid, *Appl. Mech. Rev.* **2010**, *63*, <https://doi.org/10.1115/1.4003503>.
- [17] G. Gonzalez, A. Chiappone, I. Roppolo, E. Fantino, V. Bertana, F. Perrucci, L. Scaltrito, F. Pirri, M. Sangermano, *Polymer* **2017**, *109*, 246.
- [18] B. Li, W. Liang, L. Zhang, F. Ren, F. Xuan, *Sens. Actuators, A* **2022**, *340*, 113526.
- [19] S. Kumar, T. K. Gupta, K. M. Varadarajan, *Composites, Part B* **2019**, *177*, 107285.
- [20] M. F. Arif, S. Kumar, T. Shah, *Mater. Des.* **2016**, *101*, 236.
- [21] J. Ubaid, J. Schneider, V. S. Deshpande, B. L. Wardle, S. Kumar, *Adv. Eng. Mater.* **2022**, *24*, 2200194.
- [22] P. Verma, J. Ubaid, K. M. Varadarajan, B. L. Wardle, S. Kumar, *ACS Appl. Mater. Interfaces* **2022**, *14*, 8361.
- [23] Z. Lei, Z. Chen, H. Peng, Y. Shen, W. Feng, Y. Liu, Z. Zhang, Y. Chen, *J. Mater. Sci.* **2018**, *53*, 14495.
- [24] R. Paz, R. Moriche, M. Monzón, J. García, *Polymers* **2020**, *12*, 733.
- [25] V. B. Mohan, B. J. Krebs, D. Bhattacharyya, *Mater. Today Commun.* **2018**, *17*, 554.
- [26] S. W. Kwok, K. H. H. Goh, Z. D. Tan, S. T. M. Tan, W. W. Tjiu, J. Y. Soh, Z. J. G. Ng, Y. Z. Chan, H. K. Hui, K. E. J. Goh, *Appl. Mater. Today* **2017**, *9*, 167.
- [27] K. R. Ryan, M. P. Down, N. J. Hurst, E. M. Keefe, C. E. Banks, *eScience* **2022**, *2*, 365.
- [28] M. Criado-Gonzalez, A. Dominguez-Alfaro, N. Lopez-Larrea, N. Alegret, D. Mecerreyes, *ACS Appl. Polym. Mater.* **2021**, *3*, 2865.
- [29] P. Verma, A. Schiffer, S. Kumar, *Polym. Test* **2021**, *93*, 106961.
- [30] J. Saroia, Y. Wang, Q. Wei, M. Lei, X. Li, Y. Guo, K. Zhang, *Int. J. Adv. Manuf. Technol.* **2020**, *106*, 1695.
- [31] A. Cortés, X. F. Sánchez-Romate, A. Jiménez-Suárez, M. Campo, A. Ureña, S. G. Prolongo, *Polymers* **2020**, *12*, 975.
- [32] L. M. Valencia, M. Herrera, M. de la Mata, A. S. de León, F. J. Delgado, S. I. Molina, *Polymers* **2022**, *14*, 1168.
- [33] J. Z. Manapat, J. D. Mangadlao, B. D. B. Tiu, G. C. Tritchler, R. C. Advincula, *ACS Appl. Mater. Interfaces* **2017**, *9*, 10085.
- [34] O. W. Saadi, A. Schiffer, S. Kumar, *Int. J. Adv. Manuf. Technol.* **2023**, *126*, 1965.
- [35] J. Andrew J, J. Schneider, A. Schiffer, F. Hafeez, S. Kumar, *Int. J. Mech. Sci.* **2022**, *219*, 107126.
- [36] M. Rallini, J. M. Kenny, *Modification of Polymer Properties*, Elsevier Inc., Amsterdam **2017**, pp. 47–86, <https://doi.org/10.1016/B978-0-323-44353-1.00003-8>.
- [37] L. Ma, X. Lei, S. Li, S. Guo, J. Yuan, X. Li, G. J. Cheng, F. Liu, *Sens. Actuators, A* **2021**, *332*, 113144.
- [38] T. S. Shim, S. M. Yang, S. H. Kim, *Nat. Commun.* **2015**, *6*, 6584.
- [39] H. Gojzewski, Z. Guo, W. Grzelachowska, M. G. Ridwan, M. A. Hempenius, D. W. Grijpma, G. J. Vancso, *ACS Appl. Mater. Interfaces* **2020**, *12*, 8908.
- [40] N. A. Fleck, V. S. Deshpande, M. F. Ashby, in *Proc. Royal Society A: Mathematical, Physical and Engineering Sciences*, Royal Society, UK September **2010**, pp. 2495–2516, <https://doi.org/10.1098/rspa.2010.0215>.
- [41] M. Arzhakov, *Relaxation in Physical and Mechanical Behavior of Polymers*, 1st ed., CRC Press, Florida **2019**, <https://doi.org/10.1201/9780429244520>.